Residual elastic stress−strain field and geometrically necessary dislocation density distribution around nano-indentation in TA15 titanium alloy

Dong HE, Jing-chuan ZHU, Zhong-hong LAI, Yong LIU, Xia-wei YANG, Zhi-sheng NONG

School of Materials Science and Engineering, Harbin Institute of Technology, Harbin 150001, China

Abstract: Nanoindentation and high resolution electron backscatter diffraction (EBSD) were combined to examine the elastic modulus and hardness of α and β phases, anisotropy in residual elastic stress−strain fields and distributions of geometrically necessary dislocation (GND) density around the indentations within TA15 titanium alloy. The nano-indention tests were conducted on α and β phases, respectively. The residual stress−strain fields surrounding the indentation were calculated through cross-correlation method from recorded patterns. The GND density distribution around the indentation was calculated based on the strain gradient theories to reveal the micro-mechanism of plastic deformation. The results indicate that the elastic modulus and hardness for α phase are 129.05 GPas and 6.44 GPa, while for β phase, their values are 109.80 GPa and 4.29 GPa, respectively. The residual Mises stress distribution around the indentation is relatively heterogeneous and significantly influenced by neighboring soft β phase. The region with low residual stress around the indentation is accompanied with markedly high $\langle a \rangle$ type and prismatic-GND density.

Key words: nano-hardness; stress−strain fields; geometrically necessary dislocation; nanoindentation; electron backscatter diffraction; TA15 titanium alloy

1 Introduction

TA15, whose nominal chemical component is Ti−6Al−2Zr−1Mo−1V, was developed as BT20 alloy by Russia in 1964 [1]. As a typical near α titanium, it is a classic high-temperature alloy since it combines the excellent creep behavior of α titanium alloys with the high strength of $\alpha+\beta$ titanium alloys [2]. Therefore, TA15 is preferentially used in aerospace, such as the compressor blades, compressor disks of gas turbine engine and large front fan of modern jet engines [3−5].

Generally, the microstructure of TA15 titanium consists of dominant coarse α phase (hexagonal close-packed, HCP) lamellae and a few retained β phase (body-centered cubic, BCC) layers (less than 10% in volume fraction) [1,5]. Because α is the dominant component of phase, its mechanical and plastic deformation proprieties play a decisive role in the in-service properties of TA15 titanium alloy parts. However, the plastic deformation of α and near α titanium alloys is usually poor because of relative high critical resolved stress (CRSS), low numbers of slip systems and poor symmetry for hcp lattice structure [6].

On the other hand, because of the poor symmetry of the HCP crystal structure, the crystal orientation also has a significant influence on the elastic-plastic deformation response of α phase [7]. Furthermore, although the content of β phase is relatively low, it has a significant influence on the dislocation transmission and strain−stress compatibility during the plastic deformation or forming process [8]. Therefore, it is very important to conduct deep and full mechanical response study on the α and β phases in titanium alloys.

Nanoindentation is an instrumented hardness testing technique, with precise indent location, high resolution load control and displacement measurement [9]. It is widely used to evaluate the elastic modulus, hardness, local mechanical properties, elastic-plastic responses and micro-heterogeneity properties in materials science [10,11]. Over the last two decades, electron backscattered diffraction (EBSD) has been developed to be a worldwide available and relatively easy-to-use technique to characterize the microstructure property. Actually, EBSD method not only offers the microstructure and crystal orientation information, but also can be used to study the plastic equivalent strain, Mises stress distribution at grain scale [12] and even the

dislocation content which can be calculated from the detected lattice rotations [13]. Many similar researches have been conducted to deeply understand the local deformation mechanism [14,15]. However, the orientation gradients and Nye's framework from traditional patterns indication (based on Hough transform analysis) are relatively lowly sensitive to determine the GND densities [16]. Most recently, WILKINSON et al [17] have developed the cross-correlation-based analysis of EBSD patterns which can improve the sensitivity by approximately two orders of magnitude [17].

In the present work, the nanoindention tests were performed on α and β phases of TA15 titanium alloy, respectively. The high resolution EBSD measurements were conducted on the area around the indentations and the diffraction patterns at very scanning point were recorded simultaneously. The residual elastic stress−strain fields and GND density around the indentations were calculated using the cross-correlation method and strain gradient theories. Finally, the neighboring soft β phase influence on the anisotropic distributions of residual stress−strain fields and the relationships between the residual elastic stress−strain fields and GNDs distributions were investigated and analyzed.

2 Experimental procedure and calculation method

2.1 Materials and preparation

The experimental material was commercial TA15 alloy containing 6.47% Al, 1.59% Zr, 1.45% Mo, 1.91% V, 0.038% Fe and Ti balance in mass fraction. The β-transus temperature of used TA15 titanium was around 993 °C. The microstructure consisted of coarse α (HCP) lamellae (~5 μm in thickness and 20−50 μm in length) and a few retained β (BCC) layers (~8%), as shown in Fig. 1.

A 20 mm×10 mm×8 mm cubic sample was machined from the TA15 titanium alloy bar stock. One flat surface (20 mm×10 mm) of the cubic sample was prepared for EBSD measurements and nanoindentation by standard grounding and polishing technology. A solution consisting of 90% colloidal silica (OP-S) and 10% H_2O_2 was adopted during the final polishing process.

2.2 EBSD measurements and nanoindentation tests

In the current study, pre-EBSD and post-EBSD measurement, were performed before and after nanoindentation test, respectively. The pre-EBSD measurement was conducted with 0.2 μm scanning step size to get the crystal orientation and morphology maps which were used to determine the indentation location.
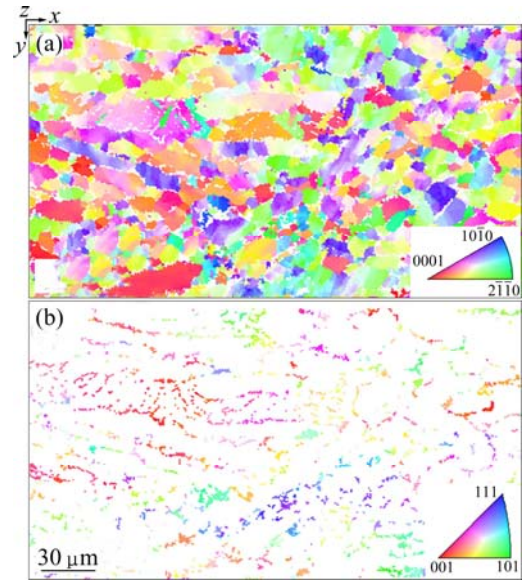

Fig. 1 Orientation map of TA15 titanium alloy in z direction with scanning step size of 0.5 μm: (a) α phase orientation map; (b) β phase orientation map

However, the post-EBSD measurement was conducted with a very fine step size (0.02 μm) to examine the crystal lattice curvatures around the indentaions. Especially, the diffraction patterns at very scanning point must be recorded simultaneously during the post-EBSD measurement for the subsequent stress−strain fields and GND density calculation. All EBSD measurements were carried out on a JEOL 6500F scanning electron microscope equipped with an EBSD system developed by EDAX/TSL®.

The nanoindentation tests were carried out in a NanoindenterXP (MTS Instruments) equipped with a diamond cono-spherica tip (1 μm tip radius, 90° cone angle). The tests were performed by the following steps. A constant displacement rate of 10 nm/s was applied until a designed indentation depth of 70 nm was reached. At the peak depth, the indenter was held at the maximum resultant load for 10 s to allow for any creep. Then, the indenter was unloaded at a constant displacement rate of 10 nm/s to 10% of the peak load. The indenter was held at this load prior to the complete uploading for further 40 s to correct thermal drift. Finally, the unloading hardness (H) and reduced elastic modulus (E_r) were calculated from the resultant unloading curves using Testworks 4.11 software. The elastic modulus of the test materials, E_s, is calculated from E_r as follows [18]:

$$E_s = (1-v_s^2)\left(\frac{1}{E_r} - \frac{1-v_i^2}{E_i}\right)^{-1} \tag{1}$$

where v_s and v_i are the Poisson ratio of the test material and indenter, respectively; E_i is the reduced elastic

modulus of the diamond indenter. Here, for a diamond indentation tip, v_i=0.07 and E_i=1140 GPa were adopted [19].

2.3 Cross correlation method and GND density calculation

The cross-correlation analysis is based on the detection of the small shifts in the positions of zone axes in the EBSD patterns. The details of calculation process and further discussion can be found in Refs. [16,17,20]. Here, the commercial software CrossCourt V3 is adopted to calculate the displacement gradient tensor and residual elastic stress−strain fields around the indentation regions.

The GND density calculation and result visualization are undertaken using routines ourselves developed within Matlab. The full description of GND theory can be found in Nye, Ashby and Kroner's work [13,21,22]. The application examples and detailed calculation steps can refer to these presentations [7,14,15,23]. For α phase in titanium alloys, there are 24 known possible independent slip systems [24]. Here, all of 33 types of potential dislocations are considered in GND density calculation, as listed in Table 1. It should be noted that different dislocation types have different line energies and contributions to lattice curvature. The different weight factors for different dislocation types used in our GND density calculation are also listed in Table 1 [7].

Table 1 Potential dislocation types in α titanium

Slip system	Burgers vector	Edge		Screw	
		Number	Weight	Number	Weight
$\langle a \rangle$-basal	$\langle 11\bar{2}0 \rangle$	3	0.124	3	0.087
$\langle a \rangle$-prismatic	$\langle 11\bar{2}0 \rangle$	3	0.124	0	−
$\langle a \rangle$-pyramidal	$\langle 11\bar{2}0 \rangle$	6	0.124	0	−
$\langle c+a \rangle$-pyramidal	$\langle 11\bar{2}3 \rangle$	12	0.437	6	0.306

3 Results and discussion

3.1 Hardness and elastic modulus

Six and three groups of nanoindentation tests were carried out on α and β phases, respectively. The indentation number and location are shown in Fig. 2. From the orientation map (Fig. 2(a)) and atomic force microscopy map (Fig. 2(b)), it is obvious that indentations 1−6 were carried out on α phase and 7−9 on β phase. The crystal orientations at positions 1−6 were very close and the load axis of the indenter was almost parallel to the [13 −3 −10 −2] crystallographic orientation on the (−1 −1 2 1) surface, as shown in Fig. 2(a). Similarly, the load axes of indentations 7−9 were approximately parallel to the [−3 10 4] crystallographic orientation on the (2 −5 14) surface, the BCC crystal frame shown in Fig. 2(a).
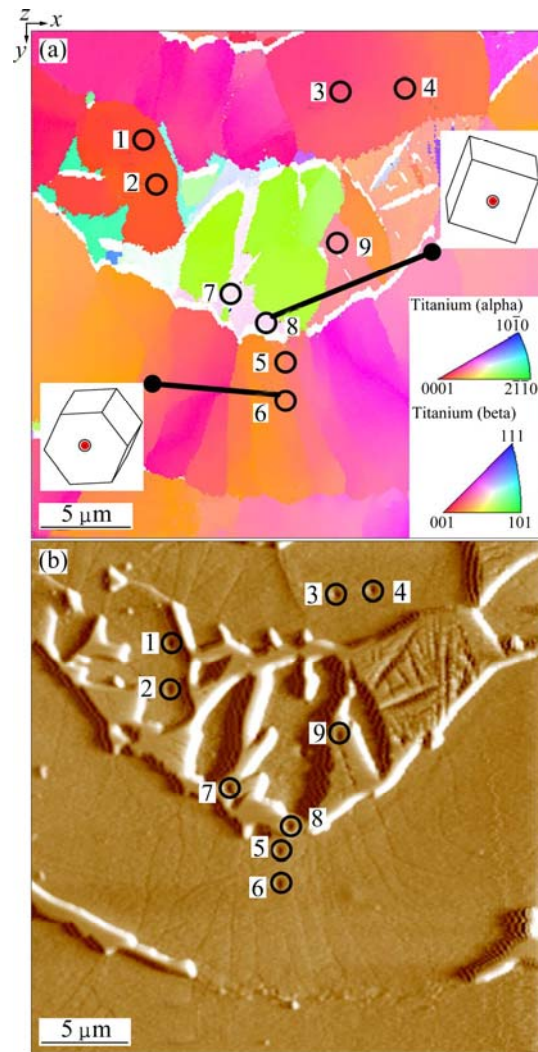

Fig. 2 Orientation map around nanoindentations with scanning step size of 0.1 μm in z direction (a) and atomic force microscopy map of nanoindentation test area (b)

The elastic modulus and hardness values of α and β phases in the TA15 titanium measured by the nanoindentation technique are presented in Figs. 3(a) and (b), respectively. The ranges of elastic modulus and hardness of α phase are 120−136 GPa and 6.0−6.87 GPa, respectively, while for β phase, the ranges are 103−115 GPa and 4.18−4.42 GPa, respectively. The elastic modulus shows obvious deviation compared with hardness distribution. The most possible reason is that the elastic modulus shows some degree of anisotropy at different crystallographic orientations [25].

The mean values and relative strand errors of elastic modulus and hardness for α and β phases are listed in Table 2. It shows that the elastic modulus and hardness of α phase are higher compared with β phase by 15% and 33%, respectively. This result means that α phase is the hard phase and bears a large fraction of total deformation during the plastic deformation process.
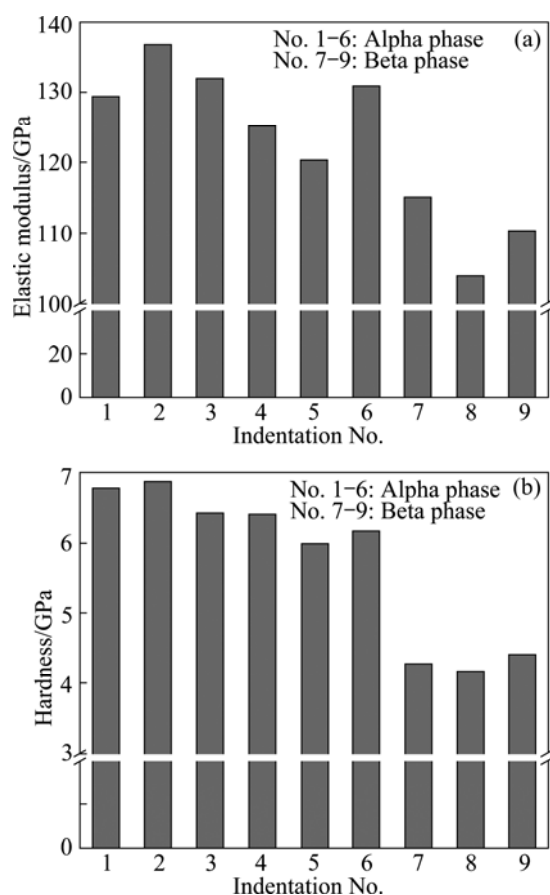
Fig. 3 Elastic modulus for α and β phases in TA15 titanium measured by nanoindentation technique (a) and corresponding hardness of α and β phases in TA15 titanium alloy (b)

Table 2 Mean values and relative standard errors of E and H for α and β phases in TA15 titanium alloy

Phase	Elastic modulus		Hardness	
	Mean/GPa	RSE*/%	Mean/GPa	RSE*/%
α	129.05	1.82%	6.44	2.11
β	109.80	2.95%	4.29	1.63

*RSE is the relative standard error (SE), calculated by SE/Mean×100%.

3.2 Residual elastic strain−stress fields around indentation

One of the indentations (No.2, as shown in Fig. 2) close to β phase was examined by SEM/EBSD with a scanning step size of 0.02 μm. The EBSD data including simultaneously recorded patterns were processed by CrossCourt software V3. The residual elastic stress−strain fields surrounding the indentation 2 were calculated based on the cross-correlation method and shown in Fig. 4.

The Mises stress distribution is relatively heterogeneous: the Mises stress value in the top-left region is significantly higher than that in the bottom-right region (separated by the black dotted line,
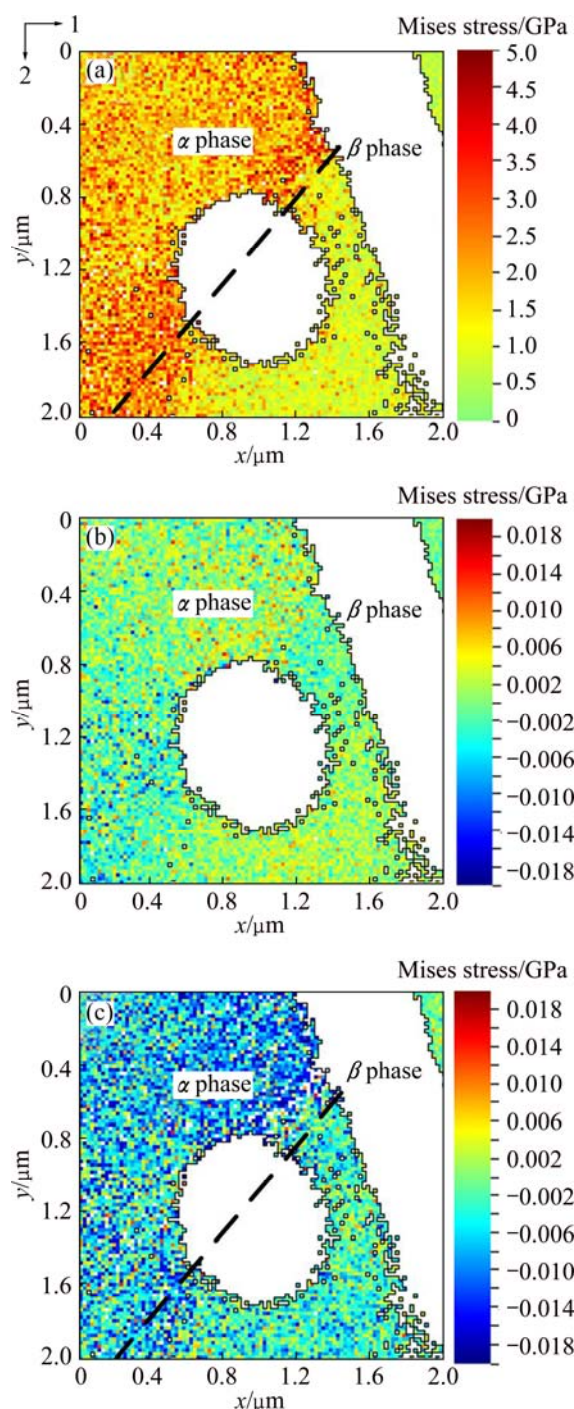

Fig. 4 Elastic stress−strain fields around indentation with region separated into two parts by black dotted line according to Mises stress: (a) Mises stress distribution; (b) E11 distribution; (c) E22 distribution

as shown in Fig. 4(a)). This resulted from the soft β phase located on the right side of indentation and inclined to vertical direction (direction 2) at an angle about of 15º. According to our experimental results in section 3.1, the β phase is softer (relatively low elastic modulus and hardness) than α phase. Therefore, some stress components, which are almost perpendicular to the

length axis of β layer, can be reduced.

The distribution of E11 (along direction 1) is much homogeneous compared with E22, as shown in Figs. 4(b) and (c). This result further validates our explanation on the Mises stress heterogeneous distribution. Because the β layer inclined to the vertical direction at ~15°, which means that it is almost perpendicular to direction 1 and paralleled to direction 2, the E11 was significantly influenced by the soft α phase and it presented relatively low value and obviously homogeneous distribution compared with E22.

3.3 GND components and density

Figure 5 shows the maps of the GND density distribution around the indentation (No. 2) region. For each map there were some points without good strain and rotation data because either the points corresponded to β phase (i.e., the top right corner), or the material was too highly deformed (i.e., indentation location in the map center).

The total GND density distribution also shows obvious heterogeneity: it is approximately 3.16×10^{16} m^{-2} within the top left region, and 3.16×10^{14} to 3.16×10^{15} within the bottom right zone. To facilitate the analysis of different type GND's contributions, the total GND density is separated into $\langle a \rangle$ and $\langle c+a \rangle$ types. The $\langle a \rangle$ type GND density and the ratio of $\langle a \rangle$ to $\langle c+a \rangle$ GND density map are presented in Figs. 5(b) and (c), respectively. It is easy to find that the $\langle a \rangle$ type GND density contributes a large factor to the total by comparing Figs. 5(a) with (b). There are two possible reasons to account for this result.

Firstly, the line energies of the GNDs are greater for $\langle c+a \rangle$ than for $\langle a \rangle$ by a factor of ~3.5 due to different magnitudes of the Burgers vectors [7]. Secondly, critical resolved shear stress values for $\langle c+a \rangle$ slip are much higher than those values for $\langle a \rangle$ GNDs [26]. However, it is also worth to pay attention that the $\langle a \rangle$ type GND density within the bottom right corner is much higher than the other regions, as shown in Fig. 5(c). This area corresponds well with the low Mises stress distribution region, as shown in   Fig. 4(a). This result indicates that the $\langle a \rangle$ type slip activation has a significant influence on reducing the residual elastic stress.

Similarly, the total GND can also be separated by different crystal planes where the dislocations stay in. The distributions of basal-GND, prismatic-GND and pyramidal-GND density are presented in Figs. 5(d), (e) and (f), respectively. The results indicate that the basal-GND density is much higher than others; indeed, the average density of basal-GND is 9.8×10^{15} m^{-2}, constituting about 60% of the total. However, although the prismatic-GND density is relatively low on average (approximately 8.2×10^{13} m^{-2}), there are regions where the prismatic-GND density is markedly higher (~4.0×10^{14} m^{-2}) than the other regions, as shown in the bottom right region in Fig. 5(e). Obviously, those regions (with markedly high prismatic-GND density) also correspond well with the low residual stress−strain locations, as shown in Fig. 4. These results demonstrate that a large number of prismatic slip system activations also promote the reduction of residual stress−strain in titanium alloys during deformation process.
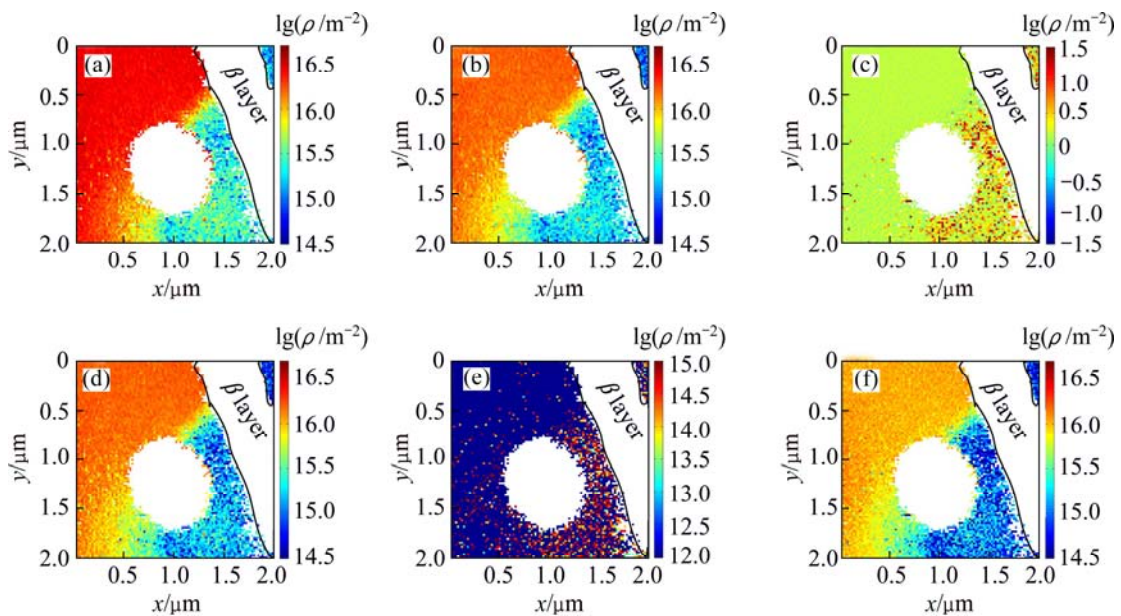

Fig. 5 HCP deconstructions of GND density around indentation (No. 2) (The color-scale is lg(ρ/m^{-2}): (a) Total GND density; (b) $\langle a \rangle$ type GND density; (c) Ratio of $\langle a \rangle$ GND density to $\langle c+a \rangle$ GND density (lg color-scale); (d) Basal-GND density; (e) Prismatic-GND density; (f) Pyramidal-GND density

4 Conclusions

1) The elastic modulus and hardness for α phase are 129.05 GPa and 6.44 GPa, while for β phase, their values are 109.80 GPa and 4.29 GPa, respectively. The elastic modulus and hardness of α phase are higher compared with β phase by 15% and 33%, respectively.

2) The distributions of the residual elastic stress−strain fields around the indentation are heterogeneous and significantly influenced by the neighboring soft β phase.

3) There is a close relationship between the residual elastic stress−strain fields and the GNDs distributions: the total GND density is remarkably high within the high residual stress regions($\sim 3.16 \times 10^{16}$ m^{-2}) compared with the other zones(3.16×10^{14}−3.16×10^{15} m^{-2}); the low residual stress regions are accompanied with dramatically high prismatic-GNDs density.

4) $\langle a \rangle$ type and basal-GND are the dominant components of GNDs for the α phase in the TA15 titanium alloy during the deformation process at room temperature. The average densities of $\langle a \rangle$ type and basal-GNDs are 1.02×10^{16} m^{-2} and 9.8×10^{15} m^{-2}, respectively, which constitute approximately 60% of the total.

References

[1]   ZHU J C, WANG Y, LIU Y, LAI Z L, ZHAN J J. Influence of deformation parameters on microstructure and mechanical properties of TA15 titanium alloy [J]. Transactions of Nonferrous Metals Society of China, 2007, 17: s490−s494.

[2]   LEYENS C, PETERS M. Titanium and titanium alloys [M]. Weinheim: Wiley-VCH Verlag GmbH & Co, 2003: 1−36.

[3]   DONACHIE M J. Titanium: A technical guide [M]. 2nd ed. Ohio: ASM International, 1988: 52−78.

[4]   WANG Z J, SONG H. Effect of high-density electropulsing on microstructure and mechanical properties of cold-rolled TA15 titanium alloy sheet [J]. Journal of Alloys and Compounds, 2009, 470(1−2): 522−530.

[5]   SUN Z C, YANG H. Microstructure and mechanical properties of TA15 titanium alloy under multi-step local loading forming [J]. Materials Science and Engineering A, 2009, 523(1−2): 184−192.

[6]   ZAEFFERER S. A study of active deformation systems in titanium alloys: Dependence on alloy composition and correlation with deformation texture [J]. Materials Science and Engineering A, 2003, 344(1−2): 20−30.

[7]   BRITTON T B, LIANG H, DUNNE F P E, WILKINSON A J. The effect of crystal orientation on the indentation response of commercially pure titanium: Experiments and simulations [J]. Proceedings of the Royal Society A: Mathematical, Physical and Engineering Science, 2010, 466(2115): 695−719.

[8]   SURI S, VISWANATHAN G B, NEERAJ T, HOU D H, MILLS M J. Room temperature deformation and mechanisms of slip transmission in oriented single-colony crystals of an alpha/beta titanium alloy [J]. Acta Materialia, 1999, 47(3): 1019−1034.

[9]   OLIVER W C, PHARR G M. Measurement of hardness and elastic modulus by instrumented indentation: Advances in understanding and refinements to methodology [J]. Journal of Materials Research, 2004,19(1): 3−20.

[10]   WU Y, WANG S Q, ZHOU D G, XING C, ZHANG Y, CAI Z Y. Evaluation of elastic modulus and hardness of crop stalks cell walls by nano-indentation [J]. Bioresource Technology, 2010, 101(8): 2867−2871.

[11]   HO E, MARCOLONGO M. Effect of coupling agents on the local mechanical properties of bioactive dental composites by the nano-indentation technique [J]. Dental Materials, 2005, 21(7): 656−664.

[12]   KAMAYA M, WILKINSON A J, TITCHMARSH J M. Quantification of plastic strain of stainless steel and nickel alloy by electron backscatter diffraction [J]. Acta Materialia, 2006, 54(2): 539−548.

[13]   KRONER E. Dislocations and continuum mechanics [J]. Applied Mechanics Reviews, 1962, 15(8): 599−606.

[14]   LIANG H, DUNNE F P E. GND accumulation in bi-crystal deformation: Crystal plasticity analysis and comparison with experiments [J]. International Journal of Mechanical Sciences, 2009, 51(4): 326−333.

[15]   KYSAR J W, GAN Y X, MORSE T L, CHEN X, JONES M E. High strain gradient plasticity associated with wedge indentation into face-centered cubic single crystals: Geometrically necessary dislocation densities [J]. Journal of the Mechanics and Physics of Solids, 2007, 55(7): 1554−1573.

[16]   WILKINSON A J, MEADEN G, DINGLEY D J. High-resolution elastic strain measurement from electron backscatter diffraction patterns: New levels of sensitivity [J]. Ultramicroscopy, 2006, 106(4−5): 307−313.

[17]   WILKINSON A J, MEADEN G, DINGLEY D J. High resolution mapping of strains and rotations using electron backscatter diffraction [J]. Materials Science and Technology, 2006, 22(11): 1271−1278.

[18]   OLIVER W, PHARR G. An improved technique for determining hardness and el astic modulus using load and displacement sensing indentation experiments [J]. Materials Research, 1992, 7(6): 1564−1583.

[19]   HAY J, PHARR G M. Instrumented indentation testing [M]. Ohio: ASM International, 2000: 232−342.

[20]   SCHWARTZ A J, KUMAR M, ADAMS B L. Electron backscatter diffraction in materials science [M]. New York: Kluwer Academic/Plenum Publishers, 2000: 231−250.

[21]   ASHBY M F. The deformation of plastically non-homogenous materials [J]. Philos Magazine, 1970, 21(1): 399−443.

[22]   NYE J F. Some geometrical results in dislocated crystals [J]. Acta Metall, 1953, 1(1): 153−162.

[23]   KYSAR J W, SAITO Y, OZTOP M S, LEE D, HUH W T. Experimental lower bounds on geometrically necessary dislocation density [J]. International Journal of Plasticity, 2010, 26(8): 1097−1123.

[24]   JONES I P, HUTCHINSON W B. Stress-state dependence of slip in titanium−6Al−4V and other H.C.P. metals [J]. Acta Metall, 1981, 29(6): 951−968.

[25]   IKEHATA H, NAGASAKO N, FURUTA T, FUKUMOTO A, MIWA K, SAITO T. First-principles calculations for development of low elastic modulus Ti alloys [J]. Physical Review B, 2004, 70(17): 1−8.

[26]   BRITTON T B, BIROSCA S, PREUSS M, WILKINSON A J. Electron backscatter diffraction study of dislocation content of a macrozone in hot-rolled Ti−6Al−4V alloy [J]. Scripta Materialia, 2010, 62(9): 639−642.

TA15 钛合金中纳米压痕附近残余应力−应变场及几何必须位错密度的分布

何 东，朱景川，来忠红，刘 勇，杨夏炜，农智升

哈尔滨工业大学 材料科学与工程学院，哈尔滨 150001

摘 要：结合纳米压痕及高分辨电子背散射衍射技术(EBSD)测定了 TA15 钛合金中 α 及 β 相的弹性模量和纳米硬度，揭示了纳米压痕附近应力−应变场及几何必须位错(GND)密度的非均匀分布情况。利用高分辨 EBSD 测试过程中同步保存的背散射电子衍射花样，并基于 cross-correlation 的处理方法，计算得出了纳米压痕附近区域的残余弹性应力−应变场分布。结合应变梯度场理论，计算分析了纳米压痕附近区域的几何必须位错密度分布，进而对合金的微观塑性变形机制进行了讨论与分析。结果表明，α 相的弹性模量及纳米硬度分别为 129.05 GPa 和 6.44 GPa，而 β 相的相应值为 109.80 GPa 和 4.29 GPa。纳米压痕附近区域的残余 Mises 应力呈现明显的非均匀分布并受到相邻较软 β 相的显著影响。压痕附近的低残余应力区域伴随有显著较高的$\langle a \rangle$形和柱面型几何必须位错密度分布。

关键词：纳米硬度；应力−应变场；几何必须位错；纳米压痕；电子背散射衍射；TA15 钛合金

(Edited by Hua YANG)